Original

Analysis of tire-road contact area in a control oriented test bed for dynamic friction models

J. Aguilar-Martínez[a], L. Alvarez-Icaza[b],*

[a]*Posgrado en Ciencias de la Ingeniería, Instituto Tecnológico de Tijuana, Tijuana, Baja California Norte, México*

[b]*Instituto de Ingeniería, Universidad Nacional Autónoma de México, México*

Abstract

The longitudinal and transversal forces distributed over the tire-road contact area are experimentally analyzed to validate the use of the lumped parameters LuGre dynamic friction model for traction-braking control purposes. To perform the analysis, a test bed based on a scaled quarter vehicle model that consists of a roller, a wheel and a servomotor was designed and built. In this device, the roller represents the road and the vehicle mass, and the tire is directly coupled to the shaft of the servomotor. The distribution of forces in the contact tire-road area is measured by means of strain gages. The obtained results show the distribution of normal forces in the tire-road contact area at different vehicle speeds. They confirmed analytic studies previously reported in the literature regarding the trapezoidal shape of the force distribution in the contact area and also allow to conclude that the lumped parameter LuGre dynamic friction models is suitable for representing the friction forces for traction-braking control purposes.

1. Introduction

The longitudinal and transversal forces on the tire-road interface largely influence vehicle dynamics (Rajamani, 2006). For this reason, a good number of studies have been conducted to propose mathematical models that describe these forces. A family of models is derived from empirical studies that use pseudo-static relationships for the tire-road forces. Some of the most notable examples of this kind of models are the so called "magic formula" (Bakker et al., 1987) and the models reported in Burckhardt (1993) and Kiencke (1993). Other approach, based on the physics of the friction phenomena, resort to dynamic friction models to describe the tire-road force interaction. The Lu-Gre dynamic friction model (Canudas et al., 1995) has received particular attention in applications for traction control because it is relatively simple and yet it describes most of the nonlinear phenomena experimentally observed in friction.

From an experimental point of view, there are several test beds used to analyze tire-road interaction (see Ginn & Marlowe, 1967; Ginn et al., 1962; Bird & Martin, 1973; Carrillo, 2004,

and I.T.V., 2006, for example). As it can be appreciated in Figure 1, that illustrates some of the typical installations, in all cases there is independent control of the tire and the rolling surface. By independently controlling the speeds of the two degrees of freedom, all possible longitudinal slips can be obtained. If force sensors are incorporated, once velocities reach a steady state, it is possible to measure the force of the tire-road interaction for each value of the longitudinal slip. Based on these mea-
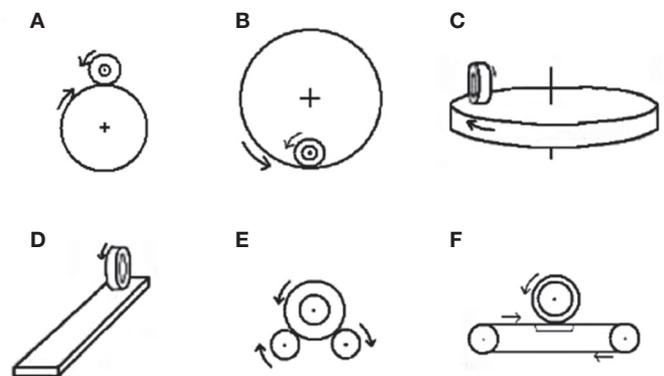

Fig. 1. Sketches of installations for analyzing tire-road force interaction.

*Corresponding author.
E-mail address: alvar@pumas.iingen.unam.mx (L. Álvarez-Icaza).

surements, force vs. slip or friction coeffcient vs. slip curves, similar to those shown in Figure 2, can be obtained. It is from these curves that most of the pseudo-static models are derived.

Pseudo-static models give only information of the total tire-road force. To analyze the force distribution in the contact patch, some authors use sensors in two manners. In the first one, sensors are placed on the tire resulting in the so called "smart tires" (Coleri et al., 2009; Castillo et al., 2006; Yilmazoglu et al., 2001). In the second case, sensors are placed below the rolling surface in such a way that normal forces in the contact area can be measured (Rose & Guenther, 2009; Muller et al., 2003; Ho et al., 2011). Sensors on the tire are normally piezo-
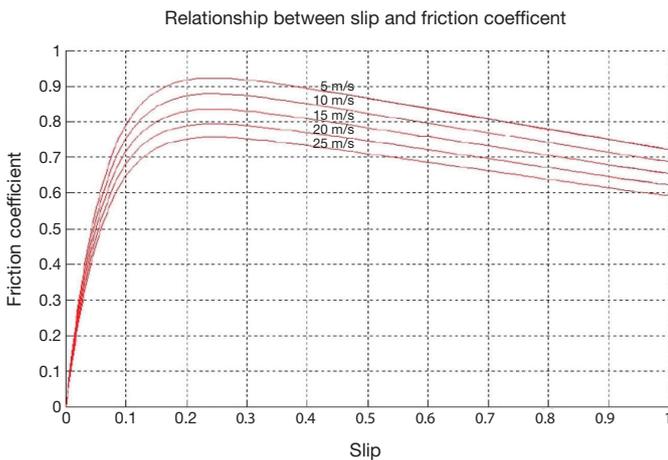
electric and therefore have limitations on their maximum size that oblige to use networks of sensor to fully cover the contact area. Sensors placed bellow the rolling surface can use piezo-electric or optical sensors and also consist in arrays of discrete sensors. Based on measurements obtained from these sensors, conclusions regarding the distribution of forces can be obtained. Recently, Zhang and Yi (2012) found that the shape of the force in the contact patch has a bimodal distribution and that force in the perimeter of the contact area is larger than inside it.

The use of LuGre model to describe the tire-road force was first introduced in Canudas and Tsiotras (1999). There are two families of LuGre models: lumped parameters and distributed parameters. Using this last one, in Tsiotras et al. (2004), a trapezoidal shape for the force distribution in the tire-road contact patch was proposed to carry out the force analysis. Distributed parameters LuGre models are difficult to use for traction-braking control purposes due to its complexity. For this reason, lumped parameters LuGre models are used instead. The formulation of these models is based on the assumption of an average behavior of forces in the contact patch area. There is, however, little experimental evidence on this average behavior of forces in the contact area and its relation with the LuGre model.

In this paper a test bed is designed and built with two initial goals: *a)* analyzing the shape of the contact forces at the tire-road interface, and *b)* validating the assumption on average force behavior for lumped parameters LuGre models. The test bed will also be used for experimenting with traction-braking control algorithms. To achieve all these goals, a different design to those used in the literature was proposed as shown in Figure 3, where it can be noticed that only the degree of freedom related

Fig. 2. Examples of slip vs. friction coefficient curves for pseudo-static models.
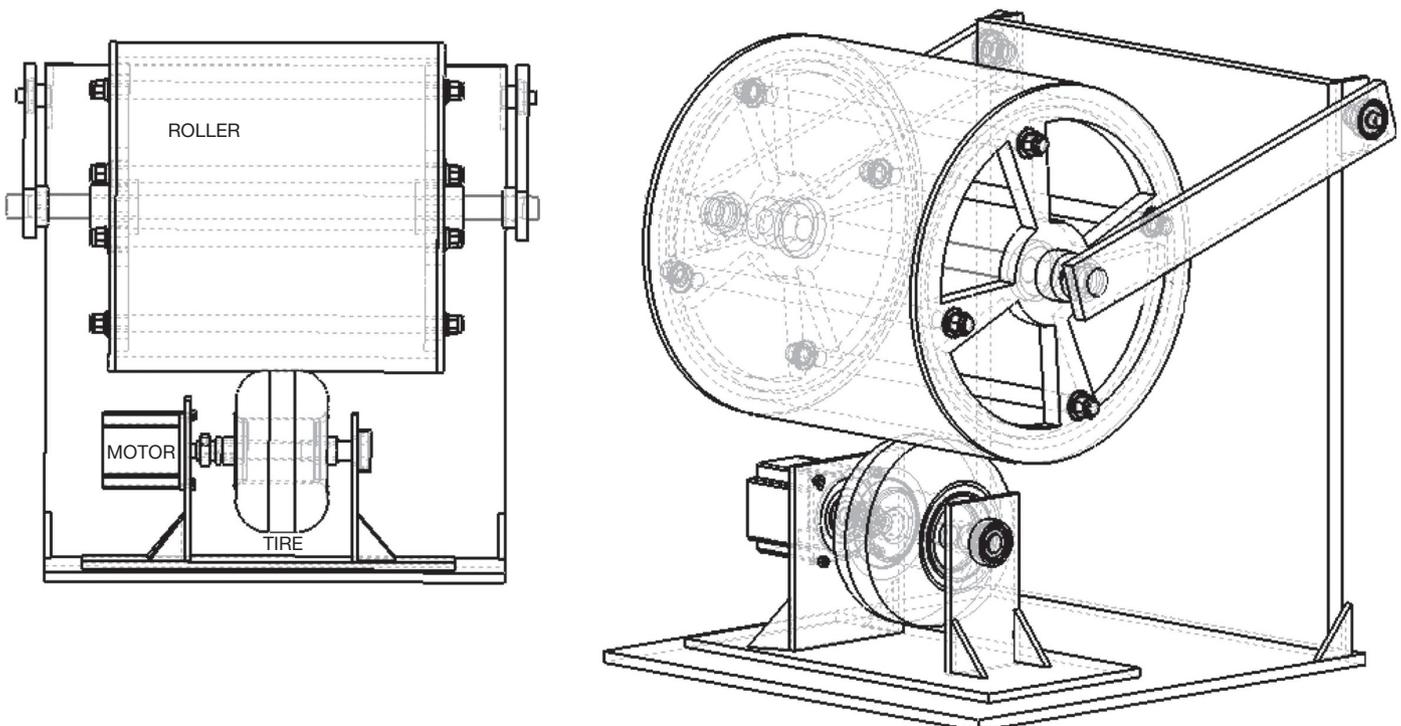

Fig. 3. Test bed design.

with the wheel is actuated by a directly coupled motor. The other degree of freedom, the rolling surface, in this case a cylinder that represents both the pavement and the vehicle inertia, it is not actuated. Its motion occurs only by the force transmitted by the tire-cylinder interface. This configuration yields an under-actuated system that, from a mechanical point of view, has an equivalent behavior of a tire-road dynamic system, as will be shown later. Another differences of this test bed with other previously designed are the type and the location of sensors. Taking advantage of their relative large size, strain gages were selected as force sensors and were directly adhered on the rolling surface. Measurements of the strain gages are processed by a wireless system as will be described later.

The paper is organized as follows. Section 2 describes the mechanical design of the test bed, while section 3 contains a review of the LuGre dynamic friction model. In section 4, the strain gages measurement system is described and section 5 explains the model for the shape of longitudinal and lateral forces distribution. Section 6 presents examples of the experimental results that are discussed in section 7. Finally, section 8 presents the conclusions and directions for future work.

Fig. 4. Equivalent quarter car vehicle model.

2. Mechanical Design of the Test Bed

The test bed design is based in a quarter vehicle model, similar to that used in Kiencke and Daiss (1994), Liu and Sun (1995), and Yi et al. (2001) given by:

$$m\dot{v} = 4F_x - F_{ax} \qquad (1)$$

where m is the vehicle mass, v the longitudinal velocity, F_x the tire-road traction-braking force and F_{ax} the aerodynamic dragging force, that can be expressed as:

$$F_{ax} = C_{ax}v^2 \qquad (2)$$

with C_{ax} the aerodynamic coeffcient, that depends on the effective exposed longitudinal area, air density and vehicle shape. The tire-road force is given by:

$$F_x = -\mu F_n \qquad (3)$$

where μ is the tire-road friction coefficient and $F_n = \dfrac{mg}{4}$ is

the normal force in each tire. The rotational dynamics of the tire is described by:

$$I_1\dot{\omega}_1 = \tau_m - \tau_b - F_x R_1 \qquad (4)$$

where $\dot{\omega}_1$ is the angular acceleration, I_1 is the tire inertia, τ_m is the driving torque, τ_b is the braking torque and R_1 is the effective tire radius.

The test bed designed to obtain data for the analysis on the tire-road contact forces consists on a roller and a tire. The roller represents the road as well as the weight of the vehicle, as seen in Figure 4, where I_2 is the inertia of the roller, I_1 is the inertia
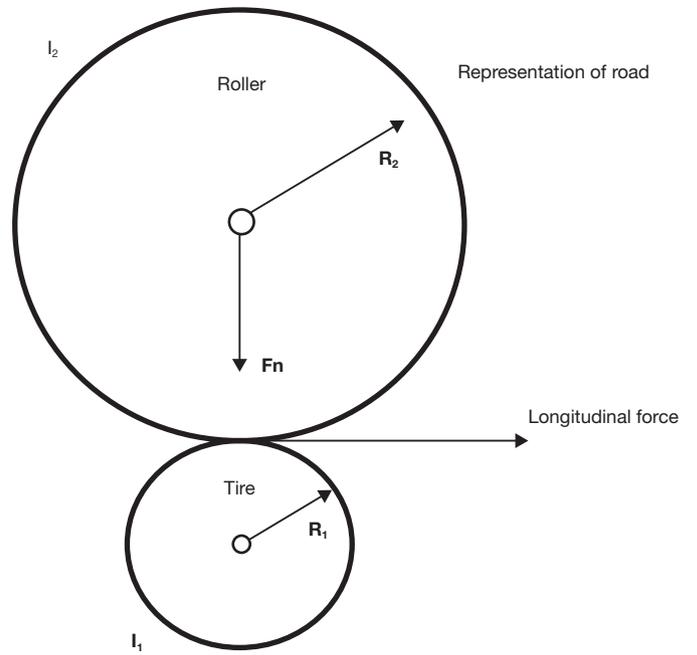
of the tire, R_2 is the ratio of the roller, R_1 is the ratio of the tire and F_n is the normal force. The roller axis of rotation is free to move in the vertical direction to guarantee that the tire is subjected to the full roller weight. The main reasons for using this design is its simplicity and the analogy with the dynamic model of the quarter vehicle.

The type of tire used is 4.5/10.0-5 DR10 and has the same basic characteristics as a conventional vehicle tire. The roller is made with high density polyethylene and its radius was chosen to make the contact between tire and roller as flat as possible. To choose the servomotor that moves the setup it is necessary to know the maximum required torque. For this purpose the relation between radius R_1 and R_2, velocities ω_1 and ω_2 and torque τ_1 and τ_2 was used.

Defining

$$r = \frac{R_2}{R_1} > 1 \qquad (5)$$

and assuming steady state, i.e., $\omega_1 R_1 = \omega_2 R_2$, Torques can be related to tire-road friction force by $F = \tau_1 R_1$ and $F = \tau_2 R_2$. The relation between torque and inertia in the tire is given by:

$$\tau_1 = \left[I_1 + \frac{I_2}{r^2}\right]\alpha_1 \qquad (6)$$

The radius of the selected wheel is $R_1 = 0.12$ [m] and the roller radius is $R_2 = 0.36$ [m]. Maximum longitudinal speed is fixed for the tire at $v_t = 13$ [m/s] and the maximum value for α_1 is set to 35.83 [rad/seg^2]. Replacing values on Eq. (6), yields:

$$\tau_1 = 4.12 \, [\text{Nm}] \qquad (7)$$

With this value, Yaskawa SGMPH servomotor, with specifications shown in Table 1, was selected. Servomotor dimensions are shown in Table 2, according to Figure 5. Once the necessary data is known, a CAD software was used for the test bed design (see Figure 3).

3. LuGre Dynamic Friction Models

The LuGre model is a dynamic friction model that can be used to describe the tire-road contact forces (Canudas & Tsiotras, 1999). In this model, it is assumed that the contact on the tire-road surface occurs through microscopic elastic bristles, following a brush analog. When a tangential force is applied, bristles deflect as a spring until sliding occurs. There are two forms for this model:

1. Distributed parameters, where the contact between surfaces is assumed to occur in a region or patch and the model represents the friction force at each differential element of area in the patch. Total force is calculated by integrating all the differential elements of force along the area of the contact patch.
2. Concentrated or lumped parameters, where an average or uniform behavior for all the elements in the contact patch is assumed. The total force is represented by a scalar quantity that is equivalent to the integration of differential forces in the contact patch for the distributed form. Figure 6 illustrates these two representations.

Distributed parameter models are of the form:

$$\delta F(\zeta,t) = \Big[\sigma_0(\zeta)\delta z(\zeta,t) + \sigma_1(\zeta)\delta\dot{z} + \sigma_2(\zeta)s\Big]\delta F_n(t) \quad (8)$$

$$\frac{d\delta z(\zeta,t)}{dt} = s - \frac{\sigma_0(\zeta)|s|}{g(s,\zeta)}\delta z(\zeta,t) \quad (9)$$

$$F = \int_0^L \delta F(\zeta,t)d\zeta \quad (10)$$

where $\delta F(\zeta,t)$ is the differential friction force at the longitudinal coordinate ζ along the contact patch and time t, $\delta z(\zeta,t)$ is internal state reflecting the deflection of bristles, s is relative velocity and δF_n is the differential of the normal force. Parameters $\sigma_0(\zeta)$, $\sigma_1(\zeta)$, and $\sigma_2(\zeta)$ are expressed per unit length and represent the stiffness and damping at position ζ. It is assumed that the contact area is constant and the normal force is evenly distributed along the contact patch that has length L, i.e.,

$\delta F_n = \dfrac{F_n}{L}$ (Canudas de Wit et al., 2003).

Function $g(s,\zeta)$ is of form:

$$g(s,\zeta) = F_c(\zeta) + \Big(F_s(\zeta) - F_c(\zeta)\Big)e^{-\left(\frac{s}{v_s(\zeta)}\right)^{\frac{1}{2}}} \quad (11)$$

that is a model to represent the "Stribeck effect," that describes the transition from a static friction force $F_s(\zeta)$ to a Coulomb friction coefficient $F_c(\zeta)$, depending on s and $v_s(\zeta)$ the "Stribeck" velocity (Canudas & Tsiotras, 1999).
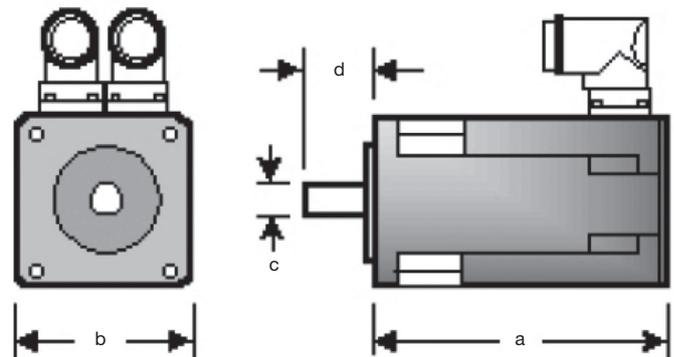

Fig. 5. Motor dimensions.

Table 1
Parameters of the technical data.

Parameter	Value	Unit
Voltage	200	[V]
Amperage	15	[A]
Torque	4.77	[Nm]
Rated output	1500 (2.01)	[W (hp)]

Table 2
Motor dimensions.

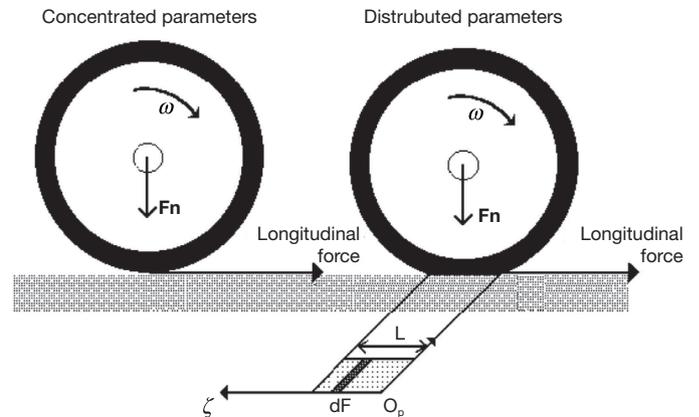| Parameter	Value	Unit
a	200	[mm]
b	80	[mm]
c	14	[mm]
d	45	[mm]

Fig. 6. Lumped model (left) and distributed (right).

There are some other friction models with distributed parameters (Dugoff et al., 1969; Tielking & Mital 1974; Dugoff et al., 1970; Rajamani, 2006), which consider the existence of variations of the contact area or footprint between the tire and the road, that are not considered here.

The lumped form of the LuGre model is given by:

$$F = \sigma_0 z + \sigma_1 \dot{z} + \sigma_2 s \qquad (12)$$

$$\frac{dz}{dt} = s - \frac{\sigma_0 |s|}{g(s)} z \qquad (13)$$

where F is the tire-road friction force, z is an internal state representing the average deflection of the bristles in the contact area and s the relative speed of motion between the surfaces, tire and road. Parameters σ_0 and σ_1 represent the average stiffness and damping of the internal state z, while σ_2 is the average viscous friction coefficient between surfaces moving at relative speed s. Finally, function $g(s)$ is of form:

$$g(s) = F_c + \left(F_s - F_c \right) e^{-\left(\frac{s}{v_s} \right)^{\frac{1}{2}}} \qquad (14)$$

that is a model to represent the average "Stribeck effect," describing the transition from an average static friction force F_s to an average Coulomb friction coefficient F_c, as a function of s and v_s the average "Stribeck" velocity (Canudas & Tsiotras, 1999).

There are two issues related with the LuGre model. The first one is related with the form of the force distribution at the contact patch. This point has been studied in Deur et al. (2001) and Velenis et al. (2002), where assuming constant parameters σ_i along the patch, calculations were made to find a trapezoidal distribution of force, similar to what is shown in Figure 7. There is not, to authors knowledge, experimental evidence that corroborates this analysis. The second issue is related to the validity of the lumped parameters form of the LuGre model. The main goals of this paper are to perform experimental work related to these two issues. The hypothesis to prove is that it is possible to utilize a dynamic friction model with lumped parameters as a good substitute for a distributed parameters models.

4. Strain Gages Measurement System

As the main purpose of this paper is to analyze the forces on the contact area between the tire and the road, it was decided to design a system with strain gages to perform this task. Strain gages are designed to measure stress or tension on concrete and other solid materials, because they can detect elongations and contractions by means of their elasto-electric properties (Ortiz et al., 2008). Strain gages were adhered to the high density polyethylene roller, longitudinally and diagonally, as shown in Figure 8.

4.1. Signal Conditioning

The circuit that was used to condition the strain gages consists on a Wheatstone Bridge, with the strain gage laid in one of the arms. In the amplification stages, two high-gain differential amplifiers for each gage and a non-inverting amplifier to amplify the output voltage were used. Amplifier gains were chosen to make the output voltage to be in the range from 0 to 5 [V] (see Figure 9).
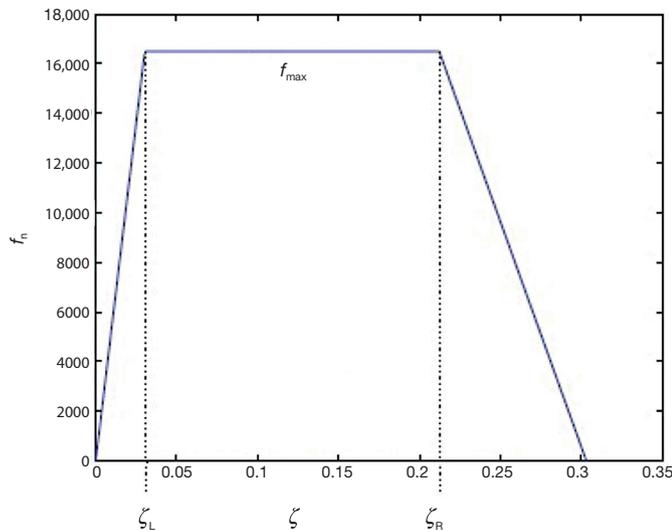

Fig. 7. Trapezoidal load distribution, f_{max} is the maximum value of the normal load distribution, ζ_L and ζ_R determine the transitions from linear to constant distribution force (Adapted from Velenis et al., 2002).
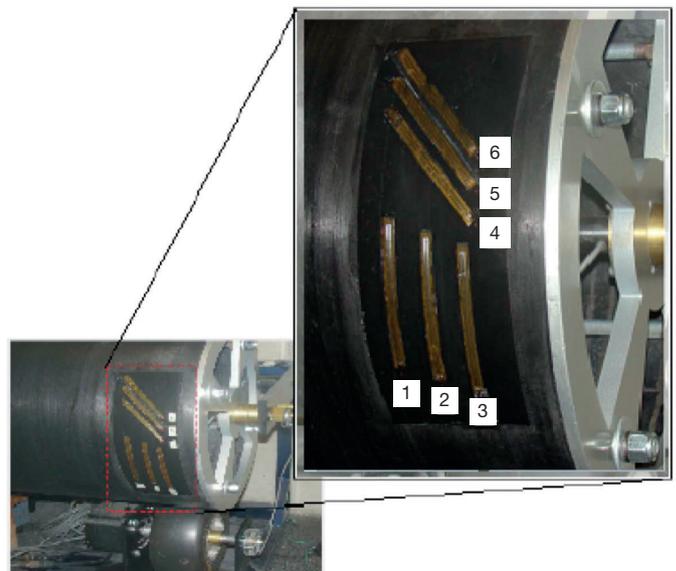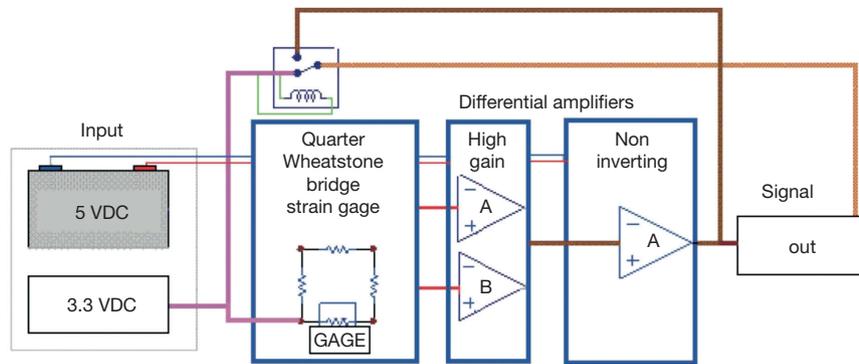

Fig. 8. Gages adhered on the roller.

Fig. 9. Diagram used for the amplification of voltage gages.

4.2. Strain Gages Foot-print

As a first step, the area covered by the contact between the strain gages and the tire was calculated. Different weights on the tire were used to produce different normal forces and the voltage in the gages was measured (Fig. 10). The area of the contact patch was obtained using carbon copy paper and using image processing ImageJ software, the average contact area was 0.0005 [m^2].

4.3. Strain Gages Frequency Response

To decide if strain gages were suitable for the task of measuring the force distribution in the contact patch, one gage was adhered to a metallic strip which was later placed on an electro-dynamic stimulator to get its frequency response. With frequencies from 20 [Hz] to 1300 [Hz], sinusoidal and square functions were programmed on the electrodynamic stimulator in order to obtain the response for the gages, that can be viewed on the Bode plot of Figure 11 where the transfer function is approximated by:

$$G(s) = \frac{1256.54}{s^2 + 157944.08}. \tag{15}$$

From the obtained results shown in Figure 11, it is clear that it is possible to use these strain gages with input frequencies smaller than 1.3×10^3 [rad/s] as the overshoot on the Bode plot indicates a resonant peak at 200 [Hz]. For inputs with $f > 200$ [Hz], the output signal of the gage has a 180° phase-shifting. In this case, 200 [Hz] is well above as the maximum speed that the roller will have, that is equivalent to 8.5 [Hz].

4.4. Wireless Communication Diagram

Once the strain gages signals were conditioned, their measurements needed to be transmitted for analysis. For this purpose, a system that consists of a microcontroller and data acquisition card was used. As the roller will be in continuous motion and not slip rings were desired, wireless communication was necessary. A Wi-Fi module and a router were used in a LAN with a single Internet IP address. The Wi-Fi module and router follow the 802.11b communication protocol and can handle data at a rate of 54 Mbps. The strain gage signals are processed by a microcontroller and send by a serial peripheral interface (SPI) to the Wi-Fi module and later received by the router, that is connected to a personal computer. Data acquisition process is done through a client-server software architecture, where the client is an application developed in JAVA language
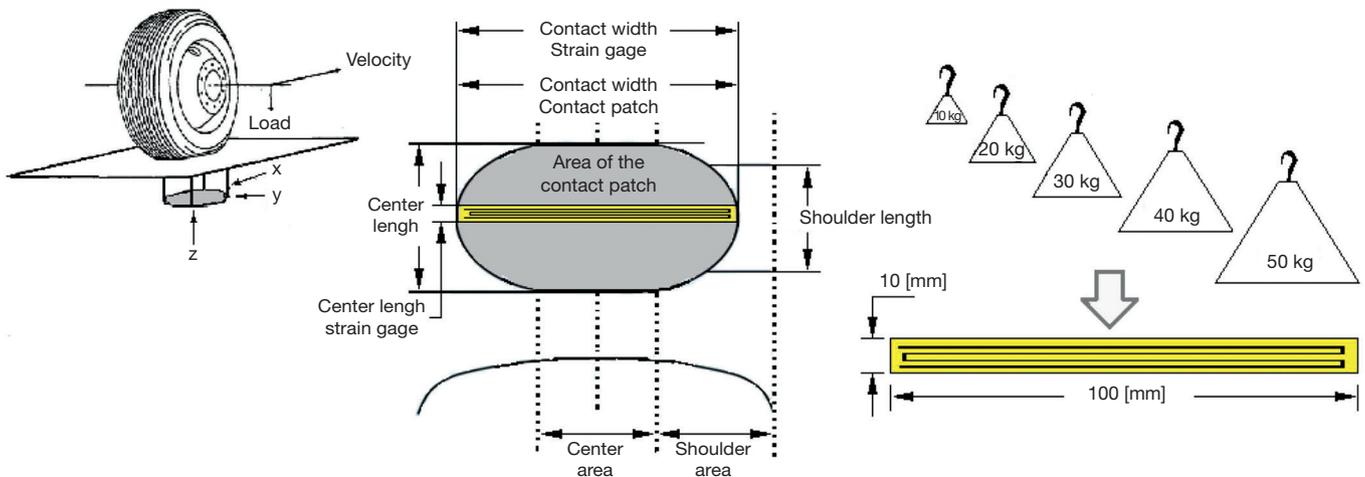

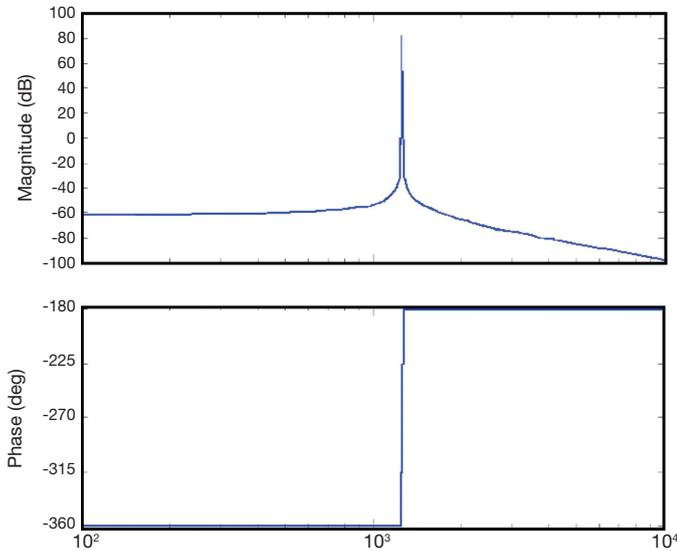Fig. 10. Area of contact covered by the strain gages.

Fig. 11. Single strain gage Bode plot.

and the server is the microcontroller. Data received by the client is stored in a database for further analysis and interpretation.

4.5. Encoders for Synchronization of Gages Measurements

To precisely know the position of the gages relative to the tire, incremental encoders were placed on the axis of the roller and of the tire. These encoders allow to know when the tire passes over the gages. For synchronization, a fixed initial position signal is sent by the encoders to allow reset of the counters in the microcontroller.

5. Longitudinal/Lateral Force Distribution

The goal of placing longitudinal and transversal of strain gages is to investigate the distribution of forces in the tire-road area of contact with the intention to confirm the shape of this distribution and to prove that for traction/control purposes lumped parameters models capture all the basic features of tire-road friction forces. The placement of the strain gages 1-6 (Fig. 8) was decided with the following rationale. Gages in the

longitudinal direction, 1-3, are intended to investigate the longitudinal force and how this force changes at different positions of the transversal direction of the tire (Fig. 12A). Gages in the diagonal direction, 4-6, measure continuous changes of the force in both the longitudinal and transversal directions (Fig. 12B). By analyzing the force patterns in the complete set of strain gages, conclusions about the force distribution can be reached.

As expected, it was found in the experiments that the distributed longitudinal and lateral forces along the contact patch are not uniform along the contact area; the shape corresponds to a polygon which resembles a trapezium, as illustrated in Figure 13, where transition points are appropriately marked. Figure 14 represents the transition points in the shape of the distribution force against the strain gage position, for gages 1-3. A similar distribution for gages 4-6 is portrayed in Figure 15.

Considering Figure 13, the function f_n that describes the longitudinal force along the patch position ζ can be approximated by piecewise functions as:

$$f_n(\zeta) = \begin{cases} \alpha_1\zeta + \beta_1 & \text{for} \quad 0 \leq \zeta \leq \zeta_1 \\ \alpha_2\zeta + \beta_2 & \text{for} \quad \zeta_1 \leq \zeta \leq \zeta_2 \\ f_{max} & \text{for} \quad \zeta_2 \leq \zeta \leq \zeta_3 \\ \alpha_3\zeta + \beta_3 & \text{for} \quad \zeta_3 \leq \zeta \leq \zeta_4 \\ \alpha_4\zeta + \beta_4 & \text{for} \quad \zeta_4 \leq \zeta \leq L \end{cases} \qquad (16)$$
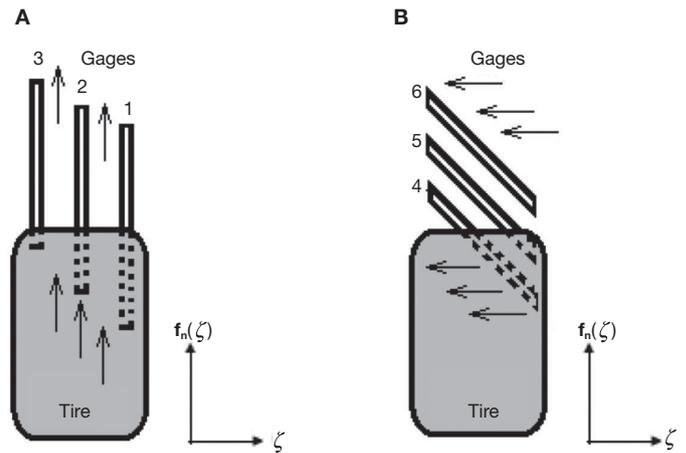

Fig. 12. Trapezoidal load distribution. A: longitudinal. B: lateral.
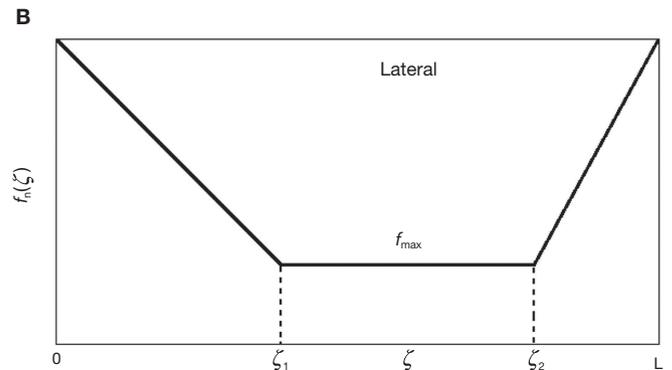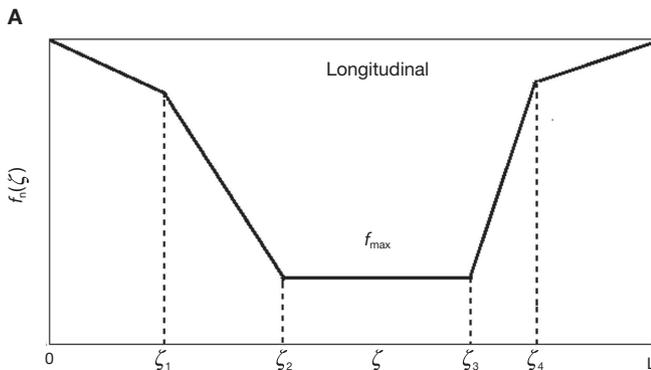

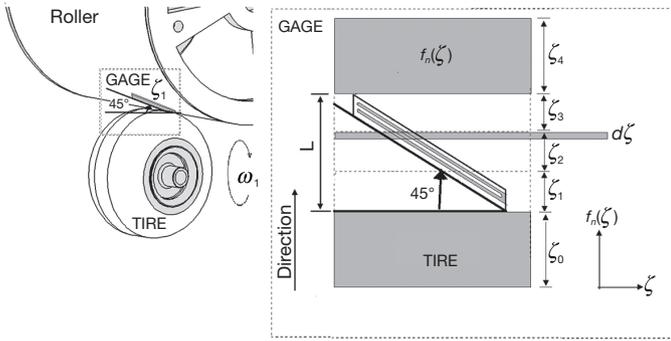Fig. 13. Trapezoidal load distribution. A: longitudinal. B: lateral.

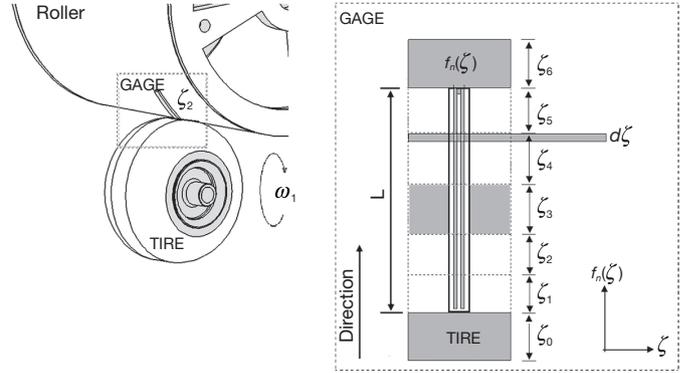Fig. 14. Representation of contact patch, longitudinal strain gages.

Fig. 15. Representation of contact patch, diagonal strain gages.

with f_{max} the maximum value of the longitudinal force, $\zeta_1, \zeta_2, \zeta_3$ and ζ_4 are the coordinates indicated in Figure 13A and:

$$\alpha_1 = \frac{f_n(\zeta_1) - f_n(0)}{\zeta_1}, \qquad \alpha_2 = \frac{f_{max} - f_n(\zeta_1)}{\zeta_2 - \zeta_1},$$

$$\alpha_3 = \frac{f_n(\zeta_4) - f_{max}}{\zeta_4 - \zeta_3}, \qquad \alpha_4 = \frac{f(L) - f_n(\zeta_4)}{L - \zeta_4},$$

$$\beta_1 = f_n(0), \qquad \beta_2 = \frac{f_n(\zeta_1)\zeta_2 - f_{max}(\zeta_1)}{\zeta_2 - \zeta_1},$$

$$\beta_3 = \frac{f_{max}(\zeta_4) - f_n(\zeta_4)\zeta_3}{\zeta_4 - \zeta_1} \qquad \beta_4 = \frac{f_n(\zeta_4)L - f_n(L)\zeta_4}{L - \zeta_4}$$

For the lateral case, force distribution f_n is approximated by:

$$f_n(\zeta) = \begin{cases} \alpha_5\zeta + \beta_5 & 0 \leq \zeta \leq \zeta_1 \\ f_{max} & \zeta_1 \leq \zeta \leq \zeta_2 \\ \alpha_6\zeta + \beta_6 & \zeta_2 \leq \zeta \leq L \end{cases} \qquad (17)$$

where transitions points correspond to Figure 13B and:

$$\alpha_5 = \frac{f_{max} - f_n(0)}{\zeta_1}, \qquad \alpha_6 = \frac{f_n(L) - f_{max}}{L - \zeta_2},$$
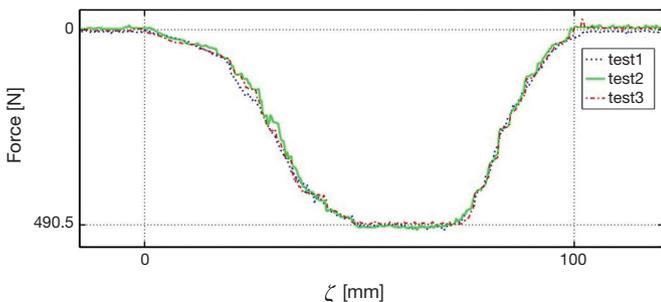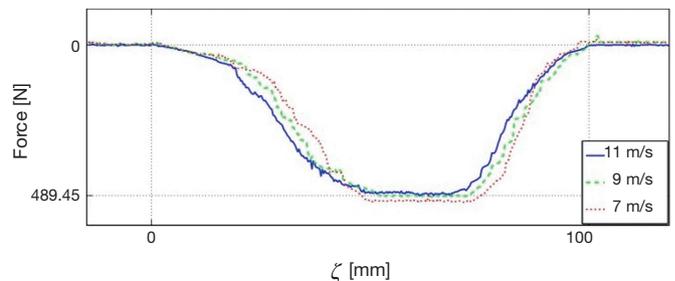
$$\beta_5 = f_n(0), \qquad \beta_6 = \frac{f_{max}L - f_n(L)\zeta_2}{L - \zeta_2}.$$

The role of these transition points will be detailed in the following sections.

6. Experimental Results

In this section the results of the experiments in the test bed equipped with the strain gages are described. All the strain gages were of the same length, 100 [mm], and have the same specifications. The normal load was kept constant and the tire was inflated to 208.8 [kPa]. The first set of results was performed with the idea of showing the repeatability of the tests. In this case, the plot in Figure 16 shows the force recorded in strain gage 1 for three different experiments executed under the same conditions of velocity. As it can be appreciated, the three experiments yielded the same results with small variations due to sensor noise.

The second set of results is shown in Figure 17, that contains the force plots for three experiments performed at different speeds. Note that, as reported in Burckhardt (1993) and Olmos and Alvarez (2005), force decreases with speed, however, the basic shape of the force distribution is similar for all speeds.

For analysis purposes, in Figure 18 the measurements of force distribution in the contact patch of gage 1 are divided into segments $\zeta_0, \zeta_1, ..., \zeta_6$. In segments ζ_0 and ζ_6 there is no tire-gage contact. Region ζ_1 is a transition where the tire begins its contact with the gage, that is not completely under the tire. For seg-

Fig. 16. Force signal from gage 1.

Fig. 17. Variations of force with speed at gage 1.

ment ζ_2 tire is in contact with the gage, however the portion of the tire making contact is composed by a compressed and a flat zone. The intermediate segment ζ_3 corresponds to full tire-roller contact. Segments ζ_4 and ζ_5 revert the behavior of regions ζ_2 and ζ_1 respectively.

Figures 19 and 20 show the behavior of gages 2 and 3, respectively. As in the case of gage 1, segments are indicated in the figure for the different types of strain gage-roller behavior.

For the gages placed in diagonal form, experiments were repeated. Figure 21 shows three tests under the same conditions for gage 4. Note that there is repeatability and that the shape of the pattern resembles the shape in Figure 13B.

This shape is different for this gage to that of the longitudinally placed strain gages. This figure shows a more linear behavior at the beginning of the contact of the tire with the gage, that is also valid for the end of the contact.

Figure 22 contains three plots of experiments with different velocities for gage 4, the observed behavior is similar to that in Figure 17, force decreases with speed. Figure 23 shows the distribution of force in the tire-road contact patch for the gage 4. This simpler pattern requires to divide the measured signal in five segments $\zeta_0, \zeta_1, ..., \zeta_4$. No contact tire-gages occurs in segments ζ_0 and ζ_6, while segment ζ_1 is a transition zone where the tire is rolling into the gages and a compression process is also happening. Segment ζ_2 is related with full tire-gage contact and, finally, segment ζ_3 reverts the process of region ζ_1. Segments for strain gages 5 and 6 are shown in Figures 24 and 25, respectively.

7. Discussion of Results

7.1. Effect of the Roller Curvature

The first point to analyze is the effect of the curvature of the roller in the length of the contact patch L that, using Figures 18-20, can be established by:
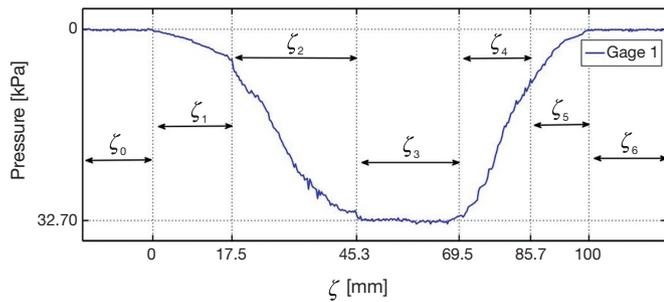

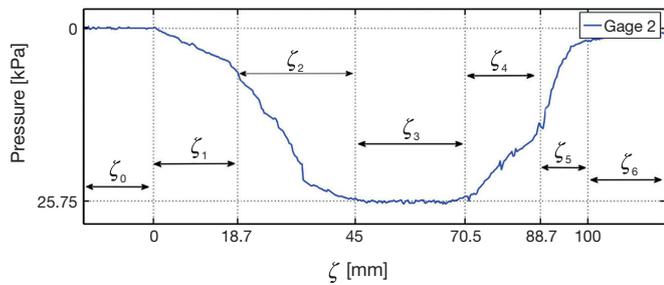Fig. 18. Force segments at gage 1 at 11 m/s speed.

Fig. 21. Force signal at gage 4.

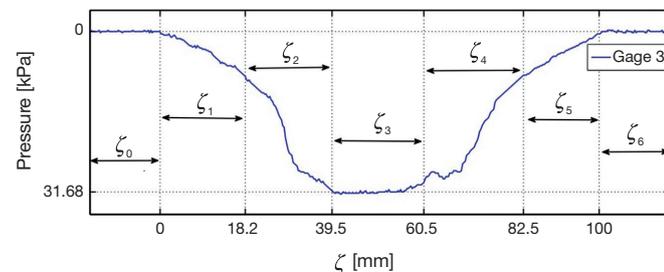Fig. 19. Force segments at gage 2 at 11 m/s speed.

Fig. 22. Variations of force with speed at gage 4.

Fig. 20. Force segments at gage 3 at 11 m/s speed.

Fig. 23. Force segments at gage 4 at 11 m/s speed.

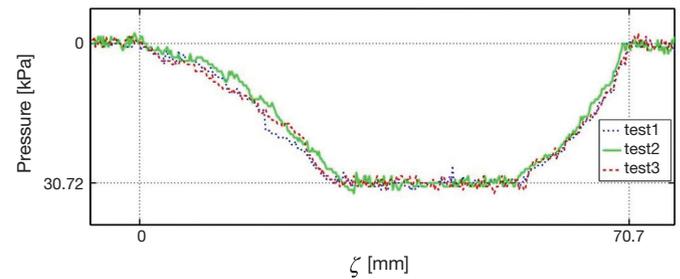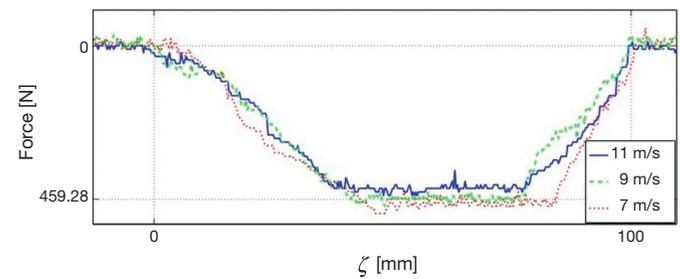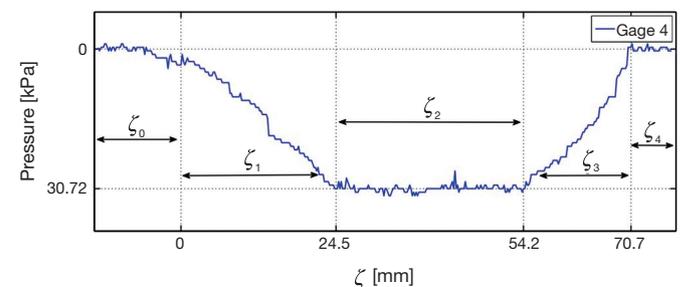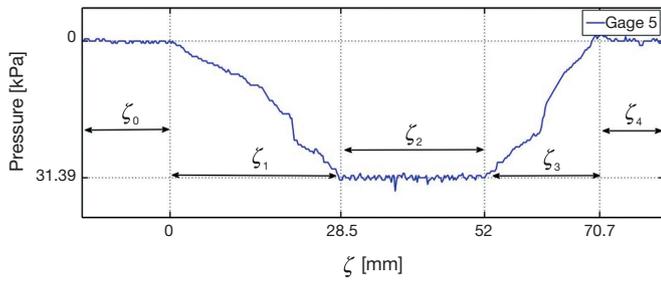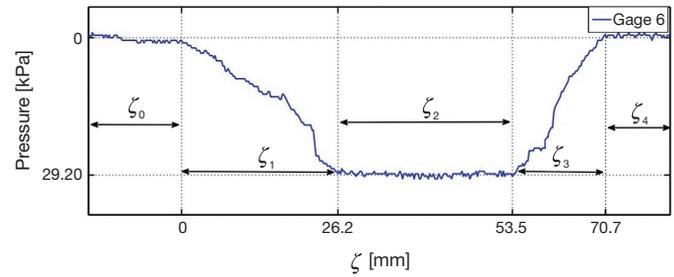Fig. 24. Force segments at gage 5 at 11 m/s speed.

Fig. 25. Force segments at gage 6 at 11 m/s speed.

$$L = \begin{cases} \zeta_3 \\ \frac{1}{2}\zeta_2 + \zeta_3 + \frac{1}{2}\zeta_4 \\ \zeta_2 + \zeta_3 + \zeta_4 \end{cases} \qquad (18)$$

depending if full contact, average contact or any contact is considered. From Figures 18-20, the value of L can be approximated to 25, 43, 61 [mm], for the three. The use of the roller introduces curvature in the contact zone, however, as the length of the contact patch is small relative to the perimeter of the roller as $2\pi R_2 = 235.5$ [mm], the average error that is introduced in the radius of contact by the curved contact of the roller is 0.06, 0.18, 0.35%, respectively, for the three lengths under consideration. These are very small values and therefore the behavior of the curved tire-roller contact can be appropriately approximated as a flat contact one.

7.2. Shape of the Contact Zone

If regions of no contact of partial tire-gage contact are discarded, that is regions ζ_0, ζ_1, ζ_5 and ζ_6 in Figures 23-25, the following conclusions can be derived.

Trapezoidal shape: The shape of the region detected by the longitudinal strain gages and marked by region ζ_2, ζ_3 and ζ_4 in Figures 18-20 is similar to Figure 7 reported in Velenis et al. (2002).

Compression and decompression zones: There is a difference in the slope of the curves that form the trapezium. Figure 7 shows that the slope of region ζ_2 is larger than the slope of region ζ_4. Experiments indicate the contrary, i.e. that the slope in region of compression ζ_2, when the tire is entering into the strain gage, is smaller than that of the region of decompression ζ_4, when the tire is leaving the strain gage.

Lateral compression: The regularity on the slope of regions ζ_2 and ζ_3 for strain gages 4, 5 and 6 shown in Figures 23-25 indicates that the compression of the tires in the lateral sense is negligible with respect to the compression in the longitudinal sense.

Size of the patch: The extension of the full contact patch, as derived from the experiments, is rectangular with an area of approximately 25 [mm] long × 18 [mm] wide and grows to 61 [mm] long × 50 [mm] wide, if partial contact is considered.

For the used tire, that has $R_1 = 133.8$ [mm] of effective radius and $W_1 = 100$ [mm] of effective width, this is equivalent to $0.18R_1 \times 0.18W_1$ and $0.45R_1 \times 0.5W_1$, respectively.

7.3. Lumped Parameters Models

The experimental results indicate that, based on the measurement at the strain gages, the friction force at the tire-roller interface is constant when full contact takes place (that corresponds to region ζ_3 in Fig. 18-20). This, in turn, implies that the lumped parameter model is a good approximation to calculate this friction force. It can be expected that the σ_1 parameters of the model in Eqs. 12-13 vary with time, when conditions in the road change. For this purpose, real time identification schemes for the parameters, as those suggested in Olmos and Alvarez (2005) can be used.

8. Conclusions

An experimental setup for analysis of the tire-road contact area was designed and constructed. This test bed is a new design proposal to directly measure the forces at the tire-road contact patch in longitudinal and lateral directions. A novel methodology to analyze the tire-road contact patch was developed. The measurement system is based on strain gages, a microcontroller and a wireless communication system. This system allowed to understand and analyze the tire-road force measurements at the contact area. Finally, experimental results confirmed the trapezoidal shape of the force distribution along the contact patch in the longitudinal direction, although with different slopes for the trapezium of those reported in the literature. The results also showed that lumped parameter LuGre dynamic friction models can correctly approximate the total force in the tire-road contact area.

References

Bakker, E., Nyborg, L., & Pacejka, H.B. (1987). *Tyre modelling for use in vehicle dynamics studies* (No. 870421). SAE Technical Paper.

Bird, K.D., & Martin, J.F. (1973). *The calspan tire research facility: design, development, and initial test results* (No. 730582). SAE Technical Paper.

Burckhardt, M. (1993). Fahrwerktechnik: Radschlupf-Regelsysteme. *Vogel-Verlag, 16*.

Canudas, C., & Tsiotras, P. (1999). Dynamic tire friction models for vehicle traction control. *Proceedings of the 38th Conference on Decision and Control. Phoenix Arizona USA.*

Canudas, C., Olsson, H., Åstrom, K., & Lischin-sky, P. (1995). A new model for control of systems with friction. *IEEE Transactions on Automatic Control, 40,* 419-425.

Canudas-de-Wit, C., Tsiotras, P., Velenis, E., Basset, M., & Gissinger, G. (2003). Dynamic friction models for road/tire longitudinal interaction. *Vehicle System Dynamics, 39,* 189-226.

Carrillo, J. (2004). *Simulación en banco de ensayo de sistemas inteligentes de frenado* (PhD Thesis). Málaga: Universidad de Málaga.

Castillo, J., Blanca, A.P.D.L., Cabrera, J.A., & Simón, A. (2006). An optical tire contact pressure test bench. *Vehicle System Dynamics, 44,* 207-221.

Coleri, S., Sangiovanni-Vincentelli, A., Sun, X., Tebano, R., Alalusi, S., Audisio, G., & Sabatini, M. (2009). The tire as an intelligent sensor. *IEEE Transactions on Computer, 28,* 941-955.

Deur, J., Asgari, J., & Hrovat, D. (2001). Dynamic Tire Friction Models for Combined Longitudinal and Lateral Vehicle Motion. *Proceedings of the ASME-IMECE World Conference: New York, USA.*

Dugoff, H., Fancher, P.S., & Segel, L. (1969). Tire performance characteristics affecting vehicle response to steering and braking control inputs. In: *Technical report, Highway Safety Research Institute, Universtity of Michigan, Ann Arbor. Final Report National Bureau of Standards Contract* (Vol. CST-460).

Dugoff, H., Fancher, P., & Segel, L. (1970). An analysis of tire traction properties and their influence on vehicle dynamics performance. In: *Proceedings FISITA Int. Auto. Safety Conference* (Vol. 700377).

Ginn, J., & Marlowe, R. (1967). *Road contact forces of truck tires as measured in the laboratory.* SAE Technical Paper 670493. doi:10.4271/670493

Ho, V., Dao, D., & Hirai, S. (2011). Development and analysis of a sliding tactile soft fingertip embedded with a microforce/moment sensor. *IEEE Transactions on Robotics, 27,* 411-424.

I.T.V. (2006). *Manual de procedimiento de inspección de las estaciones I.T.V.* (Technical report). Madrid: Ministerio de Industria, Turismo y Comercio.

Kiencke, U. (1993). Realtime estimation of adhesion characteristic between tyres and road. In: *Proceedings of the IFAC World Congress* (Vol. 1, pp. 15-22).

Kiencke, U., & Daiss, A. (1994). Estimation of tyre friction for enhaced ABS-systems. In: *Proceedings of the AVEG'94.*

Liu, Y., & Sun, J. (1995). Target slip tracking using gain-scheduling for antilock braking systems. In: *Proceedings of the 1995 American Control Conference* (Vol. 2, pp. 1178-1182). IEEE.

Muller, S., Uchanski, M., & Hedrick, K. (2003). Estimation of the maximum tire-road friction coefficient. *Journal of Dynamic Systems, Measurement, and Control, 125,* 607-617.

Olmos, L., & Alvarez, L. (2005). Optimal emergency vehicle braking based on dynamic friction model. *Journal of Applied Research and Technology, 3,* 13-25.

Ortiz Laurel, H., Rössel Kipping, D., & Debernardi de la Vequia, H. (2008). *Diseño de transductores de fuerza utilizando galgas extensométricas.* Colegio de Postgraduados. Institución de Enseñanza e Investigación en Ciencias Agrícolas. p. 156.

Rajamani, R. (2006). *Vehicle Dynamics and Control.* New York: Springer Science.

Rose, J.G., & Guenther, T.E. (2009). *Vehicle tire pavement interfacial surface pressure measurements and assessments.* Technical Report KTC09-08 FR 136-04-5F.

Tielking, J., & Mital, N. (1974). *A comparative evaluation of five tire traction models.* Interim document 6, January 1974. Highway Safety Research Institute, University of Michigan.

Tsiotras, P., Velenis, E., & Sorine, M. (2004). A lugre tire friction model with exact aggregate dynamics. *Proceedings of the 2004 American Control Conference.*

Velenis, E., Tsiotras, P., & Canudas-de-Wit, C. (2002). Extension of the lugre dynamic tire friction model to 2nd motion. In *Proceedings of the 10th IEEE Mediterranean Conference on Control and Automation-MED* (pp. 9-12).

Yi, J., Alvarez, L., Claeys, X., Horowitz, R., & Canudas de Wit, C. (2001). Emergency braking control with an observer-based dynamic tire/road friction model and wheel angular velocity information. In: *Proceedings of the 2001 American Control Conference* (Vol. 1, pp. 19-24). IEEE.

Yilmazoglu, O., Brandt, M., Sigmund, J., Genc, E., & Hartnagel, H.L. (2001). Integrated InAs/GaSb 3D magnetic field sensors for "the intelligent tire". *Sensors and Actuators A: Physical, 94,* 59-63.

Zhang, Y., & Yi, J. (2012). Tire/road stick-slip interactions: experiments and analysis. In: *Proceedings of the ASME 2012 5th Annual Dynamics Systems and Control Conference* (pp. 1-10).